SCIENTIFIC REP🞐RTS

OPEN

Tunability of Band Gap and Photoluminescence in CH$_3$NH$_3$PbI$_3$ Films by Anodized Aluminum Oxide Templates

Zhan Zhang, Min Wang, Lixia Ren & Kexin Jin

Hybrid organic-inorganic halide CH$_3$NH$_3$PbI$_3$ perovskite films are deposited on anodized aluminum oxide templates with the different pore diameters via one-step spin coating method. The obvious 0.082 eV blue shift of optical band gap is observed in films with decreasing the diameters of pores from 400 to 30 nm. And numerical simulations based on finite element modeling are carried out to represent the absorption edge and consistent with the experiment results. It is interesting that the films show the intense photoluminescence with the excitation intensity of less than 1 μW. Moreover, the photoluminescence intensity is increased with increasing pore diameters, which is attributed to the radiative recombination rate of photogenerated electrons and holes. These results pave a way for the further understanding of tunable photophysical properties of perovskite films.

During the past few years, the hybrid organic-inorganic halide perovskites solar cells (PSCs) have attracted much attention as the most ideal light absorbers because their power conversion efficiency rises from 3.8% to 22.1%[1, 2], which is incredible in such a short time compared with other solar cells, such as c-Si, thin film CIGS, SrTiO$_3$ and CdTe photovoltaic materials[3, 4]. Furthermore, these perovskites (typically, CH$_3$NH$_3$PbI$_3$) exhibit novel and intriguing physical properties, *e. g.*, large light absorption throughout the UV-Vis region, suitable band gap (~1.5 eV), small exciton binding energy (20–50 meV) and long electron-hole diffusion length (>175 μm)[5–7]. Meanwhile, a lot of efforts have been made in the crucial challenges of CH$_3$NH$_3$PbI$_3$-based solar cells, such as substituting nontoxic Sn for toxic Pb[8], improving the stability by hole-transporting layer and using a vacuum flash-assisted solution process for high-efficiency large-area PSCs[9, 10]. As we know, in the mesoporous configuration of hybrid organic-inorganic halide PSCs, mesoporous oxide films are usually used as scaffold layers, which are composed of semiconductor materials or insulators owing to the ability of perovskites to transport electrons as well as holes. Originally, the CH$_3$NH$_3$PbI$_3$ perovskites were prepared by spin-coating onto the mesoporous TiO$_2$ to form a dye-sensitized liquid solar cell in 2009[1]. Since then, mesoporous oxide materials have been usually used as scaffold layers to transport electrons and holes. In 2012, Snaith *et al.* replaced the *n*-type mesoporous TiO$_2$ with insulating mesoporous Al$_2$O$_3$ in PSCs, revealing that perovskites can be used not only as sensitizers but also as electron and hole transport layers[11]. So far, insulating Al$_2$O$_3$ materials have been widely used in PSCs. Different kinds of mesoporous scaffolds have an impact on final properties of perovskites and a high degree of preferential orientation has been detected for Al$_2$O$_3$ scaffolds[12]. Moreover, the long-term stability of PSCs would be improved with a porous Al$_2$O$_3$ buffer layer or ultrathin Al$_2$O$_3$ layers prepared by atomic layer deposition[13, 14]. Nevertheless, there is a special Al$_2$O$_3$ substrate named anodized aluminum oxide (AAO) template, which is considered to be a very useful and promising material for applications in nanotechnology because of its penetrable and highly ordered porous structure. To this day, most nanowires, nanotubes and nanoparticles have been produced successfully using AAO templates[15]. Furthermore, flexible and mechanically robust PSCs have been fabricated on plastic substrates with inverted nanocone AAO structures[16].

On the other hand, the tunable band gap is an important feature of nanocrystals, *i. e.*, band gap engineering. As we have already known, the band gap of CH$_3$NH$_3$PbI$_3$ can be adjusted by substituting Cl$^-$/Br$^-$ for I^{-}[17], Sn^{2+} for Pb^{2+} or replacing CH$_3$NH$_3^+$ with other organic cations[8, 18]. Moreover, different size of particles or nanocrystallization can also modulate the band gap. Recently, Demchyshyn *et al.* have utilized AAO nanotubes with diameters of

Shaanxi Key Laboratory of Condensed Matter Structures and Properties, School of Natural and Applied Sciences, Northwestern Polytechnical University, Xi'an, 710072, P. R. China. Correspondence and requests for materials should be addressed to K.J. (email: jinkx@nwpu.edu.cn)
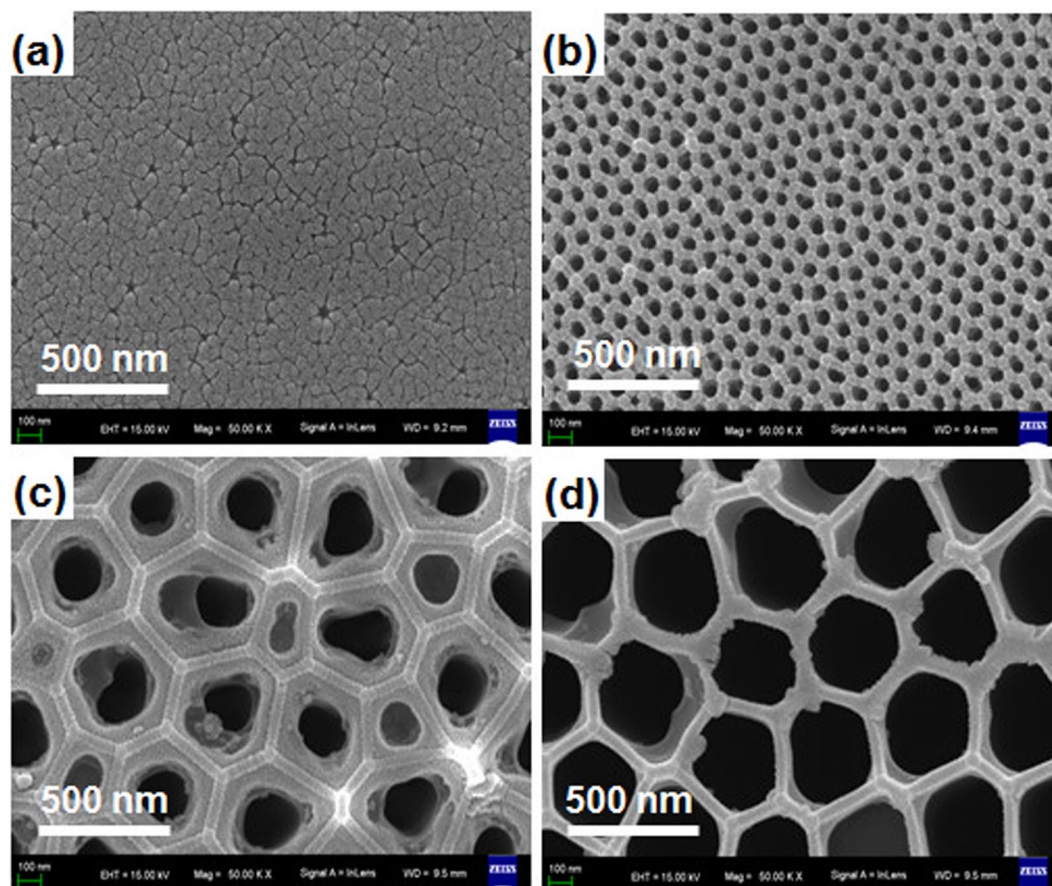
Figure 1. Top-down SEM images of the perovskite films on AAO templates with different pores in diameter: (**a**) 30, (**b**) 60, (**c**) 200, (**d**) 400 nm. In all images, scale bars are 500 nm.

6–8 nm to shift the photoluminescence peak by 62 nm on account of quantum size effect[19]. In addition, Lee *et al.* have probed crystal evolution and stability of $CH_3NH_3PbI_3$ on AAO templates with different pores in diameter[20]. Thus, it is still significant to explore their photophysical properties by changing pore diameters although the films have been prepared on AAO templates mentioned above. In this case, we deposit $CH_3NH_3PbI_3$ films via one-step spin coating method on AAO templates with the penetrable and high-ordered pores ranging from 30 to 400 nm in diameter (d_{pore}). And the structural and photophysical properties have been investigated primarily in order to have a better understanding of intrinsic mechanisms in the $CH_3NH_3PbI_3$/AAO nanostructures, which exhibit the blue shift of band gap and the reduced photoluminescence with decreasing the size of pores.

Results and Discussion

The SEM images of the top surface and cross-section morphologies of $CH_3NH_3PbI_3$ on AAO templates with different pore diameters are shown in Fig. 1 and Fig. S1, respectively. We can see that all $CH_3NH_3PbI_3$ films have discontinuous crystal grains. The film on the AAO template with $d_{pore} = 30$ nm covers the great majority of templates and produce a lot of gaps among the grains with the size of about 40 nm, compared with the pure templates (Fig. S2). The grain size of $CH_3NH_3PbI_3$ film on the AAO template with $d_{pore} = 60$ nm is about 60 nm. It is difficult to determine the accurate grain size for the films on the AAO templates with larger d_{pore}. In addition, it is obvious that the $CH_3NH_3PbI_3$ films firstly crystallize on hexagonal edges of AAO templates and the pores are not fully filled. For cross-section morphologies, the crystallization of films mainly takes place along the walls of holes. The optical images of the pure AAO template and the template after depositing the film are shown (Fig. S3). We can see that the pure AAO template is transparent with slightly yellow in color. After the film deposition, both the top and bottom surfaces become very black, also demonstrating that the AAO templates are well infiltrated with the solutions.

Figure 2 presents XRD patterns of $CH_3NH_3PbI_3$ films fabricated on AAO templates with different pore diameters. The strong diffraction peaks at 13.9°, 28.2°, 31.8° and 40.4° can be respectively assigned to (110), (220), (310) and (224) diffractions, indicating the formation of crystalline $CH_3NH_3PbI_3$[21]. In addition, the XRD patterns of $CH_3NH_3PbI_3$ films on AAO templates with $d_{pore} = 200$ and 400 nm exhibit stronger (310) and (224) diffractions compared with those with $d_{pore} = 30$ and 60 nm, which mainly show strong (110) and (220) diffractions. This indicates that different pore diameters of AAO templates would affect the crystal orientation of films to a certain extent[10]. Diffraction peak at 39.2° is attributed to PbI_2, which is not observed in $CH_3NH_3PbI_3$ film prepared on Al_2O_3 single crystal substrate (Fig. S4a). And this diffraction peak of PbI_2 on AAO template with $d_{pore} = 60$ nm is obvious. To further investigate this, we prepare other two batches of films. The first batch of films is prepared
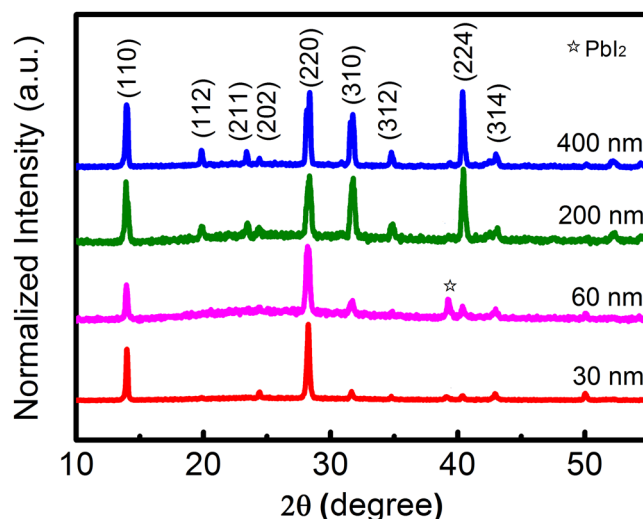
Figure 2. Comparison of XRD patterns of the perovskite films on AAO templates with different pores in diameter.

under the same condition mentioned above and the second is prepared by dipping the AAO templates in the same solution for 2 hours instead of the spin-casting method. The XRD patterns show the same results in the first batch of films (Fig. S4b). And the XRD patterns of the second batch of films show ultra-strong diffraction peak of PbI_2 for all films and it is still stronger for $CH_3NH_3PbI_3$ film on AAO template with $d_{pore} = 60\,nm$ than others (Fig. S4c). So we deduce that this phenomenon might come from the porous structure and is related to the ratio between pore and grain sizes.

Figure 3a presents the UV-vis absorption spectrum of $CH_3NH_3PbI_3$ films. High absorbance is obtained in the visible region for all the films on AAO templates. The absorption spectrum of the pure AAO templates is shown in Fig. S5. The pure AAO templates exhibit low absorption, indicating the high absorbance originates from $CH_3NH_3PbI_3$ films. According to the absorption coefficient, a tauc plot of $(\alpha h\nu)^2$-$h\nu$ is used to determine the optical band gap, as shown in Fig. 3b. And the relationship between d_{pore} and optical band gap is described in Fig. 3c. The optical band gap is increased from 1.536 eV to 1.618 eV with decreasing d_{pore} of AAO templates from 400 nm to 30 nm. Thus an obvious 0.082 eV blue shift of optical band gap is produced. In addition, the Urbach energy of the $CH_3NH_3PbI_3$ films can be obtained by fitting the absorbance curve at the optical band edge using an empirical equation[22]. As shown in Fig. 3c, the Urbach energy is proportional to the d_{pore} of AAO templates. It is known that Urbach energy is a characterization of structural disorder in the materials and higher Urbach energy is related to higher disorder. Hence, it indicates larger pores of AAO templates lead to higher disorder in $CH_3NH_3PbI_3$ films. In general, there are two mechanisms giving rise to the blue shift, including the doping effect and the quantum size effect. Obviously, the doping effect can be excluded in our work. Then the quantum size effect generally would affect the band gap. However, Bohr radius of $CH_3NH_3PbI_3$ films is about 2.2 nm calculated from the magnetoabsorption spectrum[23], and the minimum grain size obtained from the SEM patterns in our work is ~40 nm on AAO template with $d_{pore} = 30\,nm$. Thus the contribution of quantum size effect to the blue shift of our films is negligible, which is completely different from the results investigated by Demchyshyn et al.[19]. Thereby, based on finite element modeling, we carry out the investigation on numerical simulations to represent the absorption feature in wavelength range from 700 to 780 nm. The model is shown in Fig. 4a. The main physical parameters of t_{in}, t_{top}, d denote the thickness of films adhered on the inwall of the pore, the thickness of films deposited on AAO top surface, and the wall thickness of AAO, respectively. These values are estimated from the SEM images for different cases, and increasing t_{in} and decreasing t_{top} are set with increasing the d_{pore} of AAO templates (Table S1). By considering the higher order degree of the top surface and the capability of the computer, the height of AAO template is set as 1 μm. Simulation results are shown in Fig. 4b. It is clear that the whole tendency of the absorption curve agrees well with the experimental data. While the degree of the blue shift is smaller than the experimental value, which seems to result from the dielectric constant of single crystal is used in our calculation[24]. When the pore size is small and the period is short, the dispersive relationship of the structure can be equaled as a homogeneous material based on Maxwell-Garnett effective medium method. The absorption behavior can be calculated by Snell's low[25]. For the long period, the model can be regarded as a dielectric waveguide[26]. The cutoff wavelength is in direct proportion to the d_{pore}. Thus, the absorption edge is blue-shifted as the d_{pore} decreases. In additional, the minimal absorbances are different. It is because that the probability of photons coming into the waveguide becomes larger as the d_{pore} increases. The incoming photons are absorbed during propagation in the pore.

Figure 5a presents the photoluminescence (PL) spectrum of $CH_3NH_3PbI_3$ films on AAO templates with different pore diameters with a constant excitation intensity of 0.3 μW. The PL peaks as shown in Fig. 5b are consistent with that of the UV-vis peaks in Fig. 3b, which has a 14 nm blue-shift from 775 nm to 761 nm with decreasing d_{pore} of AAO templates. The PL intensity exceeds 10^4 counts with the excitation intensity less than 1 μW. Moreover, the PL intensities are increased with increasing pore diameters of AAO templates. To further
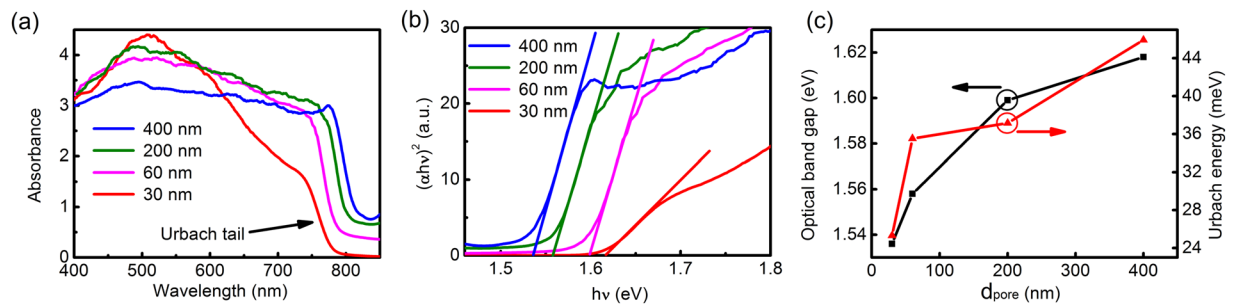
Figure 3. (**a**) UV-vis absorption spectrum of the films on AAO templates with different size of pores; (**b**) Tauc plot according to the absorption coefficient to estimate the band gap of the perovskite films; (**c**) Optical band gaps and Urbach energies of the perovskite films.
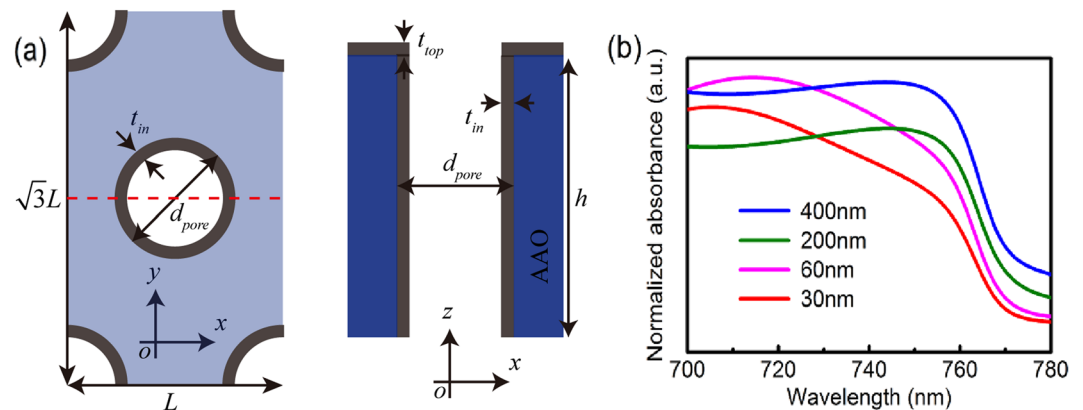

Figure 4. (**a**) Schematic diagram of finite element modeling. The dark, wathet blue and dark blue regions represent $CH_3NH_3PbI_3$ on the top surface, inwall and AAO template itself, respectively; (**b**) Simulated absorbance in the range of 700~800 nm.

examine the relationship between PL intensity (I_{PL}) and excitation intensity (I_{EX}), we measure the PL intensity of $CH_3NH_3PbI_3$ films on AAO template with $d_{pore} = 200$ nm at the excitation intensity ranging from 0.058–0.743 μW in Fig. 5c. When the excitation power intensity is higher than 0.75 μW, the PL intensity of the $CH_3NH_3PbI_3$ film would not be determined by our optical spectrometer system due to the saturation. In direct bandgap semiconductors under non-resonant excitation conditions, the I_{PL} is a power-law function of the I_{EX}, which is expressed by: $I_{PL} \propto I_{EX}^k$, where $1 < k < 2$ for recombination of excitons[27]. Figure 5d shows the PL intensity vs. excitation intensity on a double-logarithmic scale. We obtain a power-law exponent k of 1.567, which is very close to that for excitons of $CH_3NH_3PbI_3$ films on planar glass substrates[28, 29]. The intrinsic mechanism of this process is the photoneutralization of the donors/acceptors, which result in competitive recombination channels[28]. Accordingly, the $CH_3NH_3PbI_3$ film deposited on AAO template with $d_{pore} = 200$ nm has negligible effect on the choice of recombination channels. Furthermore, we attempt to measure the electrical property in plane and out-of-plane of all $CH_3NH_3PbI_3$ films on AAO templates under the same irradiation, whereas the current can not be determined due to the high resistivity. Furthermore, we draw a schematic diagram based on the band theory as shown in Fig. 6. For $CH_3NH_3PbI_3$ films, the electrons in the valence band acquire enough energy to reach the conduction band and leave holes in the valance band, forming the electron-hole pairs under the irradiation. Snaith *et al.* have considered that the morphology has essential influence to the performance of $CH_3NH_3PbI_3$-type solar cell[30]. Generally, the electron-hole pairs would generate two opposite outcomes: generating free carriers through charge dissociation or recombination (including radiative recombination and non-radiative recombination). In our study, $CH_3NH_3PbI_3$ films have discontinuous grain domains, which limit the electron-hole pairs to be free charges by charge dissociation. Thus, electrical properties are difficult to measure due to the limit of equipments. On the contrary, the electron-hole pairs emit photons by radiative recombination, resulting in the enhanced PL intensity exceeding 10^4 counts with the excitation intensity less than 1 μW. Moreover, the increasing PL intensity with increasing pore diameters of AAO templates might originate from the higher disorder of films indicated through Urbach energy mentioned above. This is similar with results in the porous TiO_2 with different pore sizes derived from the radiative recombination rate of photogenerated electrons and holes[31, 32]. Meanwhile, the k value obtained above demonstrates that our $CH_3NH_3PbI_3$ films based on AAO templates have negligible effect on the choice of recombination channels[28]. In other word, the increase of radiative recombination is caused by the decrease in the charge dissociation instead of the change between radiative recombination and non-radiative recombination. The
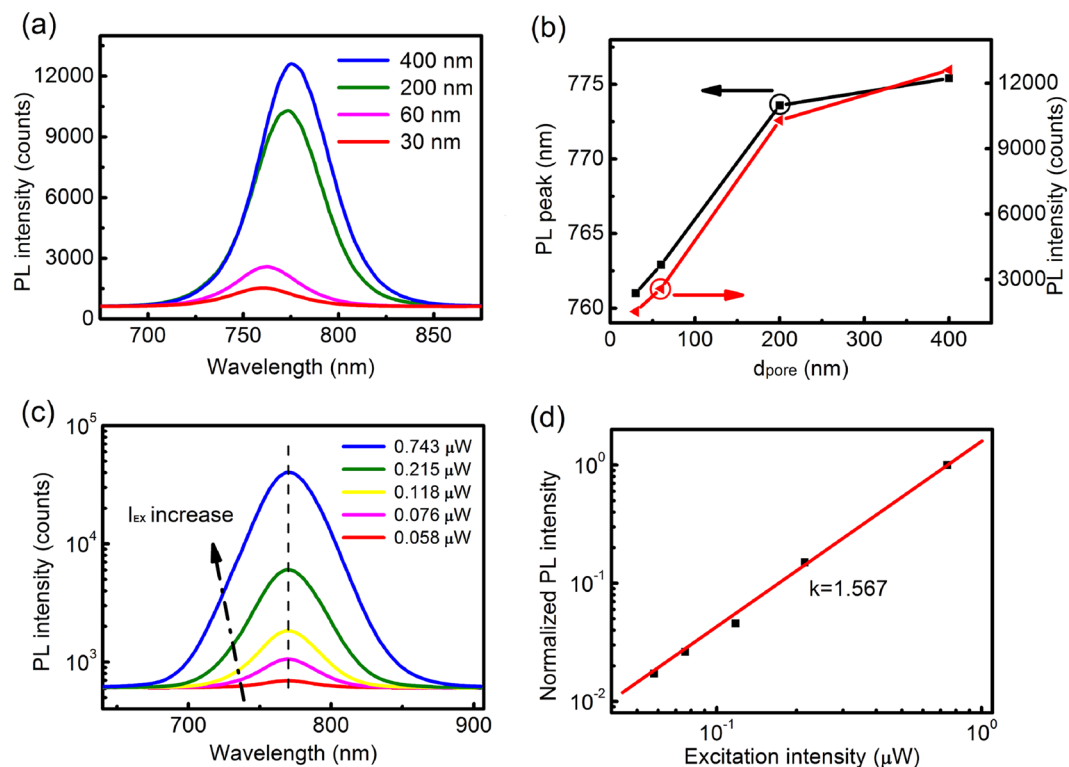
Figure 5. (**a**) PL spectra of the perovskite films on AAO templates with different size of pore; (**b**) Emission peaks and intensities of the perovskite films; (**c**) PL spectra of the perovskite film on AAO template with $d_{pore} = 200$ nm recorded with excitation intensity from 0.058 to 0.743 uW. All spectra are measured in air at room temperature. The peak energy is indicated by the dashed line; (**d**) Logarithm plot of the integrated PL intensity versus excitation intensity.
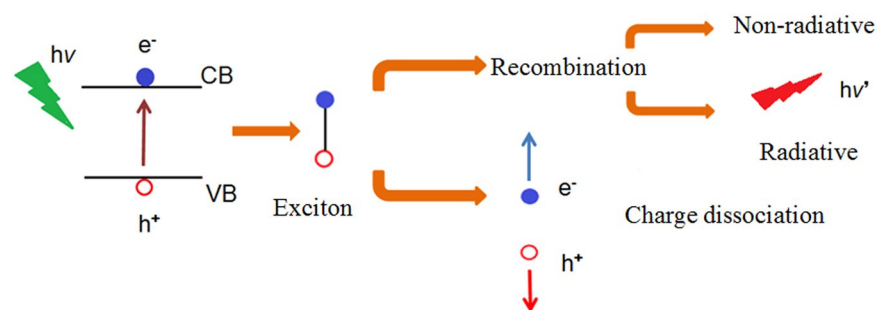

Figure 6. Schematic diagram based on the band theory shows that electron-hole pair has two opposite ways: charge dissociation or recombination (radiative and non-radiative recombination).

strong PL intensity has promising applications in light emitting devices and laser with changeable light-emission positions and intensity.

Conclusion

In summary, we have detailed the structural and photophysical properties of $CH_3NH_3PbI_3$ films fabricated on AAO templates with the pores in diameter ranging from 30 to 400 nm. Both UV-vis absorption spectrum and PL spectrum show the blue shift with decreasing pore sizes. The numerical simulations based on finite element modeling to represent the absorption edge agree well with the experiment results. And a strong linear power-law is observed in PL spectrum. In general, our work on $CH_3NH_3PbI_3$/AAO indicate the band gap of $CH_3NH_3PbI_3$ films can be tuned easily by changing the pore sizes of AAO templates, and the intense PL intensity can also be controlled readily, which can be utilized in light-emitting diode and laser.

Methods

Film preparation. CH_3NH_3I (0.163 g, 99.5% purity) was mixed with PbI_2 (0.471 g, 99.99% purity) in anhydrous N,N-dimethylformamide (1 mL) by ultrasonic shaking at 60 °C for 2 hours to produce a $CH_3NH_3PbI_3$

solution with concentration of 40 wt%. The $CH_3NH_3PbI_3$ solution was then dropped onto an AAO template (substrate diameter 12 mm). After a 20 s delay time, the template was spun cast at 5000 rpm for 40 s. The sample was then dried on a hot plate at 120 °C for 25 min. The $CH_3NH_3PbI_3$ solution was also spun cast on an Al_2O_3 substrate (substrate area 5 mm × 5 mm) under the same preparation condition as a reference. The whole process was in a nitrogen-filled glovebox.

Structure characterization. The surface and cross-section (fractured) morphology of the thin films were characterized by using a scanning electron microscope (SEM) (JSM-6700F, JEOL). X-ray diffraction (XRD) was performed using a X-ray diffractometer (XRD-7000, Shimadzu) with Cu-Kα radiation source ($\lambda = 1.5406$ Å) at a step size of 0.02°.

Photophysical characterization. The ultraviolet-visible (UV-vis) absorption spectrum was measured using an ultraviolet-visible spectrophotometer (U-3010, Hitachi). The photoluminescence (PL) spectrum of the thin films was performed with an optical spectrometer (SP-2500, Princeton Instruments) using a 532-nm radiation pulsed laser beam.

References

1. Kojima, A., Teshima, K., Shirai, Y. & Miyasaka, T. Organometal Halide Perovskites as Visible-light Sensitizers for Photovoltaic Cells. *J. Am. Chem. Soc.* **131**, 6050–6051, doi:10.1021/ja809598r (2009).
2. Green, M. A., Emery, K., Hishikawa, Y., Warta, W. & Dunlop, E. D. Solar cell efficiency tables (version 48). *Prog. Photovolt.* **24**, 905–913, doi:10.1002/pip.v24.7 (2016).
3. Jin, K. X. *et al.* Self-powered Ultraviolet Photovoltaic Effects Based on Metal/SrTiO₃ Schottky Junctions. *Europhys. Lett.* **103**, 1067–1069 (2013).
4. Jin, K. X. *et al.* Tunable Photovoltaic Effect and Solar Cell Performance of Self-doped Perovskite SrTiO₃. *Aip Adv.* **2**, 042131, doi:10.1063/1.4766279 (2012).
5. Im, J. H., Lee, C. R., Lee, J. W., Park, S. W. & Park, N. G. 6.5% Efficient Perovskite Quantum-dot-sensitized Solar Cell. *Nanoscale* **3**, 4088–4093, doi:10.1039/c1nr10867k (2011).
6. Sum, T. C. & Mathews, N. Advancements in Perovskite Solar Cells: Photophysics behind the Photovoltaics. *Energy Environ. Sci.* **7**, 2518–2534 (2014).
7. Dong, Q. *et al.* Electron-hole Diffusion Lengths >175 µm in Solution-grown CH3NH3PbI3 Single Crystals. *Science* **347**, 967–970, doi:10.1126/science.aaa5760 (2015).
8. Noel, N. K. *et al.* Lead-free Organic–inorganic Tin Halide Perovskites for Photovoltaic Applications. *Energy Enviro. Sci.* **7**, 3061–3068, doi:10.1039/C4EE01076K (2014).
9. Yan, W. *et al.* Stable High-performance Hybrid Perovskite Solar Cells with Ultrathin Polythiophene as Hole-transporting Layer. *Nano Res.* **8**, 1–7 (2015).
10. Li, X. *et al.* A Vacuum Flash-assisted Solution Process for High-efficiency Large-area Perovskite Solar Cells. *Science* **353**, 58–62, doi:10.1126/science.aaf8060 (2016).
11. Lee, M. M., Teuscher, J., Miyasaka, T., Murakami, T. N. & Snaith, H. J. Efficient Hybrid Solar Cells Based on Meso-superstructured Organometal Halide Perovskites. *Science* **338**, 643–647, doi:10.1126/science.1228604 (2012).
12. Listorti, A. *et al.* Effect of Mesostructured Layer upon Crystalline Properties and Device Performance on Perovskite Solar Cells. *J. Phys. Chem. Lett.* **6**, 1628–1637, doi:10.1021/acs.jpclett.5b00483 (2015).
13. Guarnera, S. *et al.* Improving the Long-term Stability of Perovskite Solar Cells with a Porous Al_2O_3 Buffer Layer. *J. Phys. Chem. Lett.* **6**, 432–437, doi:10.1021/jz502703p (2015).
14. Dong, X. *et al.* Improvement of the Humidity Stability of Organic–inorganic Perovskite Solar Cells Using Ultrathin Al_2O_3 Layers Prepared by Atomic Layer Deposition. *J. Mater. Chem. A.* **3**, 5360–5367, doi:10.1039/C4TA06128D (2015).
15. Schmid, G. Materials in Nanoporous Alumina. *J. Mater. Chem.* **12**, 1231–1238, doi:10.1039/b110753b (2002).
16. Tavakoli, M. M. *et al.* Efficient, Flexible and Mechanically Robust Perovskite Solar Cells on Inverted Nanocone Plastic Substrates. *Nanoscale* **8**, 4276–4283, doi:10.1039/c5nr08836d (2016).
17. Mosconi, E., Amat, A., Nazeeruddin, M. K., Grätzel, M. & Angelis, F. D. First-principles Modeling of Mixed Halide Organometal Perovskites for Photovoltaic Applications. *J. Phys. Chem. C* **117**, 13902–13913, doi:10.1021/nl5012992 (2013).
18. Eperon, G. E. *et al.* Formamidinium Lead Trihalide: A Broadly Tunable Perovskite for Efficient Planar Heterojunction Solar Cells. *Energy Environ. Sci.* **7**, 982–988, doi:10.1039/c3ee43822h (2014).
19. Demchyshyn, S. *et al.* Solid-state Nanopore Confinement for Band Gap Engineering of Metal-halide Perovskites. arXiv:1607.04661 [cond-mat.mtrl-sci] (2016).
20. Lee, S., Feldman, J. & Lee, S. S. Nanoconfined Crystallization of MAPbI₃ to Probe Crystal Evolution and Stability. *Cryst. Growth Des.* **16**, 4744–4751, doi:10.1021/acs.cgd.6b00801 (2016).
21. Etgar, L. *et al.* Mesoscopic $CH_3NH_3PbI_3$/TiO₂ Heterojunction Solar Cells. *J. Am. Chem. Soc.* **134**, 17396–17399, doi:10.1021/ja307789s (2012).
22. Urbach, F. The Long-wavelength Edge of Photographic Sensitivity and of the Electronic Absorption of Solids. *Phys. Rev.* **92**, 1324–1324, doi:10.1103/PhysRev.92.1324 (1953).
23. Tanaka, K. *et al.* Comparative Study on the Excitons in Lead-halide-based Perovskite-type Crystals $CH_3NH_3PbBr_3$, $CH_3NH_3PbI_3$. *Solid State Commun.* **127**, 619–623, doi:10.1016/S0038-1098(03)00566-0 (2003).
24. Leguy, A. *et al.* Reversible Hydration of $CH_3NH_3PbI_3$ in Films, Single Crystals and Solar Cells. *Chem. Mater.* **27**, 3397–3407, doi:10.1021/acs.chemmater.5b00660 (2015).
25. Wang, M. *et al.* Truncated spherical voids for nearly omnidirectional optical absorption. *Opt. Express* **19**, 20642–20649, doi:10.1364/OE.19.020642 (2011).
26. Taylor, J. R. *Theory of Dielectric Optical Waveguides.* 2nd ed, 367–372 (Academic Press, 1992).
27. Schmidt, T., Lischka, K. & Zulehner, W. Excitation-power Dependence of the Near-band-edge Photoluminescence of Semiconductors. *Phys. Rev. B* **45**, 8989–8994, doi:10.1103/PhysRevB.45.8989 (1992).
28. He, H. *et al.* Exciton localization in solution-processed organolead trihalide Perovskites. *Nat. Commun.* **7**, doi:10.1038/ncomms10896 (2016).
29. Wen, X. *et al.* Defect Trapping States and Charge Carrier Recombination in Organic-inorganic Halide Perovskites. *J. Mater. Chem. C* **4**, 793–800, doi:10.1039/C5TC03109E (2016).
30. Eperon, G. E., Burlakov, V. M., Docampo, P., Goriely, A. & Snaith, H. J. Morphological Control for High Performance, Solution-processed Planar Heterojunction Perovskite Solar Cells. *Adv. Funct. Mater.* **24**, 151–157, doi:10.1002/adfm.v24.1 (2014).
31. Niu, J. *et al.* Synthesis and Photoactivity of Anatase Porous Single Crystals with Different Pore Sizes. *Ceram. Int.* **41**, 11936–11944, doi:10.1016/j.ceramint.2015.06.005 (2015).
32. He, Z., Zhu, Z., Li, J. & Wei, N. Characterization and Activity of Mesoporous Titanium Dioxide Beads with High Surface Areas and Controllable Pore Sizes. *J. Hazard. Mater.* **190**, 133–139, doi:10.1016/j.jhazmat.2011.03.011 (2011).

Author Contributions

Z. Z. and K. J. conceived the study; Z. Z. and L. R. did the most of experiments; Z. Z., M. W. and K. J. analyzed the data and wrote the manuscript.

Additional Information

Supplementary information accompanies this paper at doi:10.1038/s41598-017-02144-x

Competing Interests: The authors declare that they have no competing interests.

Publisher's note: Springer Nature remains neutral with regard to jurisdictional claims in published maps and institutional affiliations.